IEEE Access
Multidisciplinary | Rapid Review | Open Access Journal

Received 13 September 2022, accepted 17 September 2022, date of publication 22 September 2022,
date of current version 30 September 2022.

Digital Object Identifier 10.1109/ACCESS.2022.3208564

RESEARCH ARTICLE

Novel ABC–Variable Based Closed-Form Analytical Model of Surface Mounted Permanent Magnet AC Machines With Sinusoidal and Non-Sinusoidal Back-EMF

SALEH O. EDHAH, (Student Member, IEEE), JAMAL Y. ALSAWALHI, (Senior Member, IEEE), AND ABDUL R. BEIG, (Senior Member, IEEE)

Advanced Power and Energy Center, Department of Electrical Engineering and Computer Science, Khalifa University, Abu Dhabi, United Arab Emirates

Corresponding author: Saleh O. Edhah (saleh.edhah@ku.ac.ae)

This work was supported by the Khalifa University of Science and Technology under Advanced Power and Energy Center (APEC) under Award RC2-2018-06 and Award FSU-2018-11.

ABSTRACT This work presents a novel *abc*-based model applicable to surface-mounted permanent magnet AC (SM-PMAC) machines with sinusoidal and non-sinusoidal back-electromotive force (back-emf). It is capable of predicting the electromagnetic performance metrics such as torque waveforms, machine inductances, flux linkages and back-emf. The closed form expressions of the model, which can be evaluated with a high computational efficiency, are derived from basic geometric and winding parameters. Validation of the model is carried out numerically and experimentally with a very good match in results. Finally, the computational efficiency of the model is highlighted by considering a multi-objective evolutionary optimization design of SM-PMAC machine with a relatively large number of design parameters, where results are presented and discussed.

INDEX TERMS AC motors, analytical model, electric machines, permanent magnet motors, park transformation, multiple reference frame transformation (MRFT).

I. INTRODUCTION

Permanent Magnet AC (PMAC) machines stand out when it comes to electric machines with high-power density and high-power conversion efficiency. They have been used in a wide variety of applications such as electric vehicles, variable speed air-conditioning systems and robotics. While designing a PMAC machine for a given application, the electromagnetic performance metrics, such as torque waveform, back-electromotive force (back-emf), and flux linkages, are captured using two common approaches; namely numerical models with finite element analysis (FEA) and analytical models. The accuracy of predictions made from FEA was shown to be comparable to experimental measurements [1], [2], [3], [4]. However, this method suffers from computational inefficiency and it might be impractical to use in the initial stages of the design when many iterations are required to study the variation of different parameters on the machine performance [5], [6].

Analytical models on the other hand can be convenient for this purpose as they are much faster to evaluate and their accuracy has been steadily improving [5], [7], [8], [9], [10], [11], [12]. For instance, in [7], a high-speed permanent magnet synchronous machine (PMSM) was designed using an analytical model that in addition to the electromagnetic performance; it could predict important thermal and mechanical metrics. A machine with a very good match between predicted and experimental measurements was designed and tested. In [8], an analytical model of cogging torque in PMSMs was developed. This model was capable of capturing the airgap flux density with results comparable to FEA considering eccentricity in the rotor or defects in the magnets. It took just 15 seconds to solve the analytical model in contrast to one hour in FEA.

The associate editor coordinating the review of this manuscript and approving it for publication was Yilun Shang.

Sub-domain models were also applied for analyzing electric machines in a number of research work [13], [14], [15], [16], [17]. In these methods, the machine is divided into sub-regions where Maxwell's equations are developed in each and boundary conditions are imposed to take the interfaces into account. One example is to divide a machine into three regions: Region 1 includes the magnets, Regions 2 includes the airgap and Region 3 includes the stator steel. By solving Poisson and Laplacian equations in these regions considering the boundary conditions set by the interfaces of the regions; an accurate expression of the airgap flux density as function of radius and rotor position could be obtained [13]. Nevertheless, sub-domain models analysis suffers from high complexity and can be time-consuming where the time required to solve the model was comparable to the time needed for an FEA simulation in [14].

Analytical models for PMAC machines often rely on Park's transformation which transforms *abc* time-varying variables into *qd* time-invariant variables that are easier to analyze [18]. An important assumption made when applying Park's transformation was that a sinusoidal back-emf existed. Yet, this is not always the case for certain subclasses of PMSMs such as Brushless Direct Current (BLDC) PMSM and Vernier Motors, where the back-emf is not sinusoidal [19]. The Multiple-Reference Frame Transformation (MRFT) was proposed to handle such situations and allow obtaining a time-invariant model. An average value model was often added to completely eliminate rotor position dependency in the transformed set of variables [20]. MRFT was applied to non-linear drive control [21], accurate estimation of torque ripple [22], and core loss calculation [23]. However, models relying on MRFTs may require applying numerical integrations and taking the derivative of a number of equations which can affect the computational time. This is important especially when integrating an analytical model with an evolutionary optimization algorithm to design PMAC machines as was done in [24], [25], and [26].

Accordingly, this work presents a novel *abc*-variable based analytical model for PMAC machines with sinusoidal or non-sinusoidal back-emf. The main contributions of this work are highlighted below:

- Closed form expressions are presented to facilitate the calculations of machine parameters such as torque waveform, inductances and voltages. Hence no need to apply any numerical integrations or differentiations, which enhance the evaluation speed and computational efficiency.
- The analytical model presented is valid for PMAC machines with sinusoidal and non-sinusoidal back-emf. Therefore, it very suitable to be used in an evolutionary optimization design algorithm where the variation in the degrees of freedom may result in one of these two classes of PMAC machines; raising the need for a general model that can handle both cases.
- The model presented is simpler and faster than previously reported models based on MRFTs and sub-domain analysis, and therefore can be easily applied to analyze a given PMAC machine.

The organization of this paper is as follows. In Section II the model is presented and derived in terms of basic machine geometrical and winding parameters. In Section III the model is validated using numerical and experimental measurements on a lab-scale prototype. In Section IV, the model is used in an evolutionary multi-objective optimization environment to demonstrate its effectiveness from a computational perspective. In Section V, the conclusion and future work drawn from this work are presented.

II. MACHINE DESIGN

The proposed model is derived and explained in this section. In this derivation, the following assumptions were made. First, the magneto-motive force (MMF) drop across the steel is negligible. Second, only the radial component of the airgap flux density is considered, the tangential and axial components are neglected due to their negligible magnitude. Third, the three-phase stator currents are assumed to be balanced and harmonic free. Lastly, tooth-tips in the stator teeth are ignored and the teeth are assumed to have a rectangular geometry.

A. GEOMETRY

A developed diagram of a surface-mounted PMAC machine, which shows a portion of it redrawn in a linear fashion, is shown in Fig. 1. The spatial mechanical position of the machine ϕ_{sm} is defined with respect to the stator reference axis located at the center of Stator Tooth 1 (ST1). Based on this, the rotor position θ_{rm} is defined as the displacement with respect to the stator reference axis. Note that blue sections indicate magnets whose flux points radially outward from rotor to stator, while red sections are the magnets with flux pointing radially inward from stator to rotor. Each magnet spans a mechanical angle θ_{pm} given by

$$\theta_{pm} = \alpha_{pm} \frac{2\pi}{P_r} \tag{1}$$

where P_r is the number of magnet poles and α_{pm} is a fraction between 0 and 1, controlling the circumferential span of the magnets. Some additional crucial parameters to the design and optimization process that are labeled in Fig. 1, are the depths of the stator back-iron d_{sb} and teeth d_{tb}, the depth of the rotor back-iron d_{rb}, the depth of the magnets d_m, airgap length g, the depth of the inert region d_i between shaft and rotor and the radius of rotor shaft r_{rs}. Each stator tooth has a uniform width w_{tb}. Using these variables, a number of parameters such as mass and volume of different components can be derived [27], [28]. A more detailed geometrical description of the machine can be found in [18].

B. STATOR WINDING FUNCTION

The stator winding distribution for each phase can be expressed using the winding function, which is a continuous function giving the number of turns around each stator tooth.

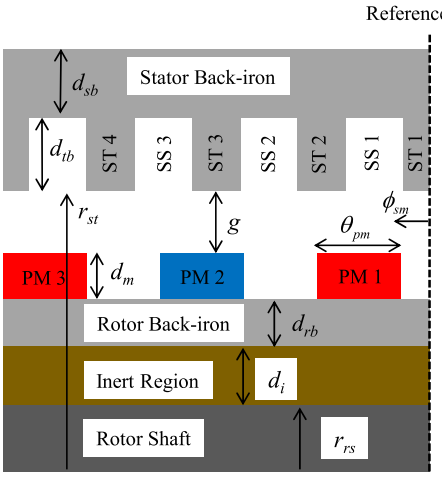

FIGURE 1. Generic developed diagram of a PMSM at zero rotor position.

The a-phase winding function can be expressed as

$$\mathrm{w}_{as}\left(\phi_{sm}\right) = w_k \cos\left(k\left(\frac{P_s}{2}\phi_{sm} + \gamma\phi_{shift}\right)\right) \tag{2}$$

where w_{as} is a-phase continuous winding function, k is an odd harmonic positive integer, w_k is the series coefficient of harmonic k, P_s is the number of stator electromagnetic poles and ϕ_{shift} is the phase angle shift between the phases. For a balanced three-phase systems with an abc sequence, ϕ_{shift} is equal to 0 for a-phase, $-120°$ for b-phase, and $+120°$ for c-phase. It should be noted that (2) is generic and can be applied to both concentrated winding and sinusoidally distributed winding distributions. To ensure that the phase shifts applied in b- and c-phases with respect to the main working harmonic is such that an abc sequence is established, parameter γ is added, which is set to 1 or -1 according to the condition explained in [27]. Note that the series summation over k is not shown in (2) for clarity.

C. STATOR WINDINGS AND MAGNETS MMFS

The a-phase current can be expressed as

$$\mathrm{i}_{as}\left(\theta_{rm}\right) = \sqrt{2}\, I_s \cos\left(\frac{P_r}{2}\theta_{rm} + \phi_i\right) \tag{3}$$

where I_s is the rms current and ϕ_i is the current vector position angle. Based on (2) and (3), and considering a balanced three-phase system, the stator MMF, F_s, can be expressed as the dot product between the three-phase currents and three-phase winding functions

$$\mathrm{F_s}\left(\phi_{\mathrm{sm}}, \theta_{\mathrm{rm}}\right) = \begin{bmatrix} \mathrm{i_{as}}\left(\theta_{\mathrm{rm}}\right) & \mathrm{i_{bs}}\left(\theta_{rm}\right) & \mathrm{i_{cs}}\left(\theta_{\mathrm{rm}}\right) \end{bmatrix} \times \begin{bmatrix} \mathrm{w_{as}}\left(\phi_{\mathrm{sm}}\right) \\ \mathrm{w_{bs}}\left(\phi_{\mathrm{sm}}\right) \\ \mathrm{w_{cs}}\left(\phi_{\mathrm{sm}}\right) \end{bmatrix} \tag{4}$$

where $\mathrm{i_{as}}$, $\mathrm{i_{bs}}$, and $\mathrm{i_{cs}}$ are the a-phase, b-phase, and c-phase currents, respectively; and $\mathrm{w_{as}}$, $\mathrm{w_{bs}}$, and $\mathrm{w_{cs}}$ are the a-phase, b-phase, and c-phase winding functions, respectively. A closed-form expression for (4) is presented in [27] and [28] for concentrated winding and sinusoidally distributed winding distributions; respectively.

The MMF due to the rotor magnets can be expressed using an odd function as

$$\mathrm{F_{pm}}\left(\phi_{sm}, \theta_{rm}\right) = f_{pm,n} \sin\left(n\frac{P_r}{2}\left(\phi_{sm} - \theta_{rm}\right)\right) \tag{5}$$

where n is the magnet MMF odd positive harmonic number, and $f_{pm,n}$ is the harmonic component given by

$$f_{pm,n} = \frac{d_m}{\mu_0\mu_r}\left(\frac{4B_r}{n\,\pi}\right)\sin\left(n\frac{\pi}{2}\right)\sin\left(n\,\alpha_{pm}\frac{\pi}{2}\right) \tag{6}$$

with μ_0 is the vacuum permeability, μ_r is the magnet relative permeability and B_r is the residual flux density. Note that the summation sign to represent the series is omitted for clarity here and in the following equations.

D. AIRGAP PERMEANCE FUNCTION

The flux passing from rotor to stator or vice versa can contain both radial and tangential components around the circumference of the machine as indicated in Fig. 2. For the instance shown in Fig. 2 (a), and assuming a relatively small airgap, the flux is dominantly radial. However, for the instance of Fig. 2 (b), the airgap flux does not flow in a straight path in the region where the permanent magnet is not fully under the span of a stator tooth.

Therefore, as presented in [29] and [30], the maximum possible airgap depth to which the flux can reach in a stator slot (SS), d_{fmx}, depends on the width of the slot w_{so}, the depth of the magnets d_m and their relative permeability μ_r, and the length of the airgap g. It can be expressed as

$$d_{fmx} = \left(g + d_m\mu_r^{-1}\right)\left(\sqrt{1 + \left(\frac{w_{so}}{2\left(g + d_m\mu_r^{-1}\right)}\right)^2}\right) \tag{7}$$

Hence, and as demonstrated in Fig. 2, it is possible to define an effective tooth depth d_{tb}^* representing the maximum depth of the slot the flux travels before emerging to the teeth given by

$$d_{tb}^* = d_{fmx} - \left(g + d_m\mu_r^{-1}\right) \tag{8}$$

Based on the previous analysis, the airgap permeance variation shown in Fig. 2 can be expressed using the Permeance function as

$$P_g\left(\phi_{sm}\right) = p_{dc} + p_{ac_j}\cos\left(j\frac{S_s}{2}\phi_{sm}\right) \tag{9}$$

where j is an even positive integer, S_s is the number of stator teeth, and p_{dc} and p_{ac_j} are the dc and ac harmonic components, respectively; given by the following two expressions

$$p_{dc} = P_{g\,\min} + \left(P_{g\,\max} - P_{g\,\min}\right)\alpha_t \tag{10}$$

$$p_{ac_j} = \frac{4}{j\pi}\left(P_{g\,\max} - P_{g\,\min}\right)\sin\left(\frac{j}{2}\alpha_t\pi\right) \tag{11}$$

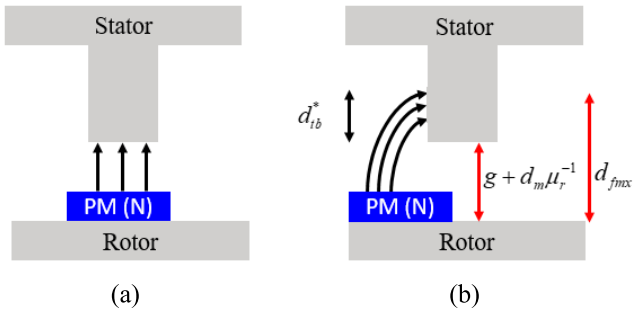

FIGURE 2. Section of a machine showing airgap flux when a magnet is (a) fully under a stator tooth, (b) partially under a stator tooth.

where α_t is a fraction, theoretically in the range of 0 and 1, controlling a stator tooth angular span θ_t. This angle along with $P_{g,\min}$and $P_{g,\max}$ are defined as

$$\theta_t = \alpha_t \frac{2\pi}{S_s} \tag{12}$$

$$P_{g,\min} = \left(\frac{\left(r_{st} + d^*_{tb}\right)}{\mu_0} \ln\left(1 + \frac{g + d_m + d^*_{tb}}{r_{rb}}\right)\right)^{-1} \tag{13}$$

$$P_{g,\max} = \left(\frac{r_{st}}{\mu_0} \ln\left(1 + \frac{g + d_m}{r_{rb}}\right)\right)^{-1} \tag{14}$$

where r_{st} is the radius to a stator tooth, and r_{rb} is the radius to the outer region of the rotor back-iron.

Based on (4), (5) and (9), and using a radial field analysis [27], [28], the airgap flux density spatial and temporal distribution at any radius r between the outer rotor back-iron and stator teeth tips can be predicted using

$$\mathrm{B_g}\left(r, \phi_{sm}, \theta_{rm}\right) = \frac{r_{st}}{r} P_g\left(\phi_{sm}\right)\left(\mathrm{F_s}\left(\phi_{sm}, \theta_{rm}\right) + \mathrm{F_{pm}}\left(\phi_{sm}, \theta_{rm}\right)\right) \tag{15}$$

E. INDUCTANCES

Considering a balanced three-phase system, the *abc* inductances can be obtained utilizing the following expression

$$L_{xx}\left(\theta_{rm}\right) = \frac{\mu_0 r_{st} l}{n_{pw}^2} \int_0^{2\pi} \frac{w_{xs}\left(\phi_{sm}\right) w_{xs}\left(\phi_{sm}\right)}{g_v\left(\phi_{sm}, \theta_{rm}\right)} d\phi_{sm} \tag{16}$$

where l is the stack length of the machine, w_{xs} is the x-phase winding function, n_{pw} is the number of parallel windings per phase and g_v is the airgap variation function that describes the variation of the airgap around the circumference of the machine, as explained in [31]. Expressions similar to (16) were presented previously but assumed that the airgap is spatially uniform [19]. In this work, to increase the accuracy; the spatial variation is also considered. Using Fourier series, this function can be expressed as an even function given by

$$\mathrm{g_v}\left(\phi_{sm}, \theta_{rm}\right) = g_{dc} + g_{ac,h} \cos\left(h \frac{P_r}{2}\left(\phi_{sm} - \theta_{rm}\right)\right) \tag{17}$$

where h is an even positive harmonic number, and g_{dc} and g_h are the dc and ac harmonics components, respectively; given by [31]

$$g_{dc} = g + d_m\left(1 - \alpha_{pm}\right) \tag{18}$$

$$g_{ac,h} = \left(\frac{-4 d_m}{h\pi}\right) \sin\left(h\,\alpha_{pm}\,\frac{\pi}{2}\right) \cos\left(h \frac{\pi}{2}\right) \tag{19}$$

The inverse of (17) is defined as e_v, which can be shown to be equal to

$$e_v\left(\phi_{sm}, \theta_{rm}\right) = e_{dc} + e_{ac,h} \cos\left(h \frac{P_r}{2}\left(\phi_{sm} - \theta_{rm}\right)\right) \tag{20}$$

in which e_{dc} and $e_{ac,h}$ are the dc and ac harmonic components given by

$$e_{dc} = e_1 + e_2 \alpha_{pm} \tag{21}$$

$$e_{ac,h} = \frac{4}{h\pi} e_2 \sin\left(h \alpha_{pm} \frac{\pi}{2}\right) \cos\left(h \frac{\pi}{2}\right) \tag{22}$$

with e_1 and e_2 are given by

$$e_1 = \frac{1}{\left(g + d_m\right) c_{s,\min}} \tag{23}$$

$$e_2 = \left(\frac{1}{g c_{s,\max}} - \frac{1}{\left(g + d_m\right) c_{s,\min}}\right) \tag{24}$$

where $c_{s,\max}$ and $c_{s,\min}$ indicate the maximum and minimum values of Carter's coefficient, respectively; as described in [32]. Note that the maximum occurs under a slot, while the minimum occurs under a tooth. Upon substituting (2) and (20) into (16) for each phase, and considering the fundamental $h = 2$, the three-phase self-inductances can be evaluated. It can be shown that the a-phase self-inductance is given as

$$L_{asm} = L_{ls} + L_{dc} + L_{ac} \cos\left(2\left(\frac{P_r}{2} \theta_{rm}\right)\right) \tag{25}$$

where L_{ls} is the self-leakage inductance considering both slot-windings and end-windings leakages as detailed in [18], L_{dc} and L_{ac} are the dc and ac-components of the self-inductance given by the following two expressions

$$L_{dc} = \frac{\left(\mu_0\, r_{st}\, l\, N_{pc}^2\right)}{n_{pw}^2} \left(e_{dc}\ \pi\right) w_s \tag{26}$$

$$L_{ac} = \frac{\left(\mu_0\, r_{st}\, l\, N_{pc}^2\right)}{n_{pw}^2} \left(e_{ac,2}\ \frac{\pi}{2}\right) w^2_{\left(\frac{P_r}{P_s}\right)} \tag{27}$$

where N_{pc} is the number of turns per coil and w_s is obtained by squaring the coefficient w_k for each harmonic and then summing them as follows

$$w_s = \sum_1^k w_k^2 = w_1^2 + w_2^2 + \ldots + w_k^2 \tag{28}$$

Similar expressions can be obtained for b-phase and c-phase with the appropriate phase shifts. In the same manner, applying (16) for the mutual inductances between any two phases, expressions for the mutual inductances can be

obtained. For instance, the mutual inductance between the a-phase and b-phase is given by

$$L_{abm} = L_{mdc} + L_{ac}\cos\left(P_r\theta_{rm} - \gamma\frac{2\pi}{3}\right) \tag{29}$$

where L_{mdc} is the dc component of the mutual-inductances defined by

$$L_{mdc} = \frac{\left(\mu_0 r_{st} l N_{pc}^2\right)}{n_{pw}^2}(e_{dc}\pi)\, w_s \sum_{k=1,2,..}\left(\cos\left(k\frac{2\pi}{3}\right)\right) \tag{30}$$

F. THREE-PHASE FLUX LINKAGES AND VOLTAGES

The a-phase flux linkage can be calculated using the following expression

$$\lambda_{as} = (L_{asm} + L_{ls})\, i_{as} + L_{abm} i_{bs} + L_{acm} i_{cs} + \lambda_{as,pm} \tag{31}$$

where $\lambda_{as,pm}$ is the a-phase open circuit flux linkage, which can be evaluated as

$$\lambda_{as,pm} = r_{st} l \int_0^{2\pi} \mathrm{w_{as}}\,(\phi_{sm})\,\mathrm{B_{pm}}\,(\phi_{sm}, \theta_{rm})\, d\phi_{sm} \tag{32}$$

where $\mathrm{B_{pm}}$ is the airgap flux density due to permanent magnets only. Substituting expression (15) with F_s set to zero into (32) and evaluating gives

$$\lambda_{as,pm} = \frac{\pi r_{st}\, l N_{pc} f_{pm,n}}{n}\left[\begin{array}{l} w_{\left(n\frac{P_r}{P_s}\right)} p_{dc} \\ +\frac{1}{2} w_{\left(\frac{S_s - \frac{P_r}{2}}{\frac{P_s}{2}}\right)} p_{ac.j} \end{array}\right] \times \sin\left(n\frac{P_r}{2}\theta_{rm}\right) \tag{33}$$

By the same procedure, the b- and c-phases can be evaluated with appropriate phase-shifts. Note that in (31)- (33) the dependence on θ_{rm} is not expressed on the left-hand side for clarity.

Substituting (3), (25), (33) and the corresponding b- and c-phase currents, self-inductances and mutual inductances into (31) and evaluating; the total a-phase flux linkage is found to be

$$\lambda_{as} = \sqrt{2} I_s \left(\begin{array}{l} L_m \cos\left(\frac{P_r}{2}\theta_{rm} + \phi_i\right) \\ +\frac{3}{2} L_{ac} \cos\left(\frac{P_r}{2}\theta_{rm} - \phi_i\right) \end{array}\right) + \lambda_{as,pm} \tag{34}$$

where $L_m = (L_{dc} - L_{mdc} + L_{ls})$. Similarly, b-phase and c-phase total flux linkages can be evaluated.

With the previous total flux linkages, the three-phase voltages can be found as per the following equation

$$v_{xs} = R_s i_{xs} + \frac{d\lambda_{xs}}{dt} \tag{35}$$

where R_s is the stator winding dc-resistance. Substituting and solving for each phase considering only the fundamental of the airgap permeance, $j = 2$, and the fundamental of the magnets MMF, $n = 1$, yields the following expressions for a-phase voltage

$$v_{as} = v_{a,R} + v_{a,L} + v_{a,B} \tag{36}$$

$$v_{a,R} = \sqrt{2} I_s R_s \cos\left(\frac{P_r}{2}\theta_{rm} + \phi_i\right) \tag{37}$$

$$v_{a,L} = \frac{-\sqrt{2}}{2} I_s P_r \omega_{rm}\left[\begin{array}{l} L_m \sin\left(\frac{P_r}{2}\theta_{rm} + \phi_i\right) \\ +\frac{3}{2} L_{ac} \sin\left(\frac{P_r}{2}\theta_{rm} - \phi_i\right) \end{array}\right] \tag{38}$$

$$v_{a,B} = \frac{\pi}{2} r_{st}\, l N_{pc} f_{pm,1} P_r \omega_{rm}\left[\begin{array}{l} p_{dc} w_{\left(\frac{P_r}{P_s}\right)} \\ +\frac{1}{2} w_{\left(\frac{S_s - \frac{P_r}{2}}{\frac{P_s}{2}}\right)} p_{ac.2} \end{array}\right] \times \cos\left(\frac{P_r}{2}\theta_{rm}\right) \tag{39}$$

where $v_{a,R}$, $v_{a,L}$, and $v_{a,B}$ are the voltage drop across the winding resistance, voltage drop across the self-inductance, and the back-emf, respectively; ω_{rm} is the rotor mechanical speed, $f_{pm,1}$ is the fundamental component of the magnets MMF, and $p_{ac.2}$ is the fundamental component of the airgap permeance function.

G. TORQUE WAVEFORM

The co-energy of the system, assuming magnetic linear conditions, is given by

$$W_c = \frac{1}{2}\mathbf{i}_{abcs}^T \mathbf{L}_s \mathbf{i}_{abcs} + \mathbf{i}_{abcs}^T \boldsymbol{\lambda}_{abcs,pm} + W_{pm} \tag{40}$$

where W_{pm} is coupling field energy due to the permanent magnets. The electromagnetic torque as a function of rotor position can be found by taking the derivative with respect to rotor mechanical position

$$T_e\,(\theta_{rm}) = \frac{\partial W_c}{\partial \theta_{rm}} \tag{41}$$

Substituting the expressions for currents (3), inductances (16), and magnet flux linkages (32) into (40), and from (41); the torque expression can be obtained. It can be shown that the torque expression can be segregated into two terms: a constant independent of rotor position term T_L which stems from the first term on the right-hand side of (40), and coefficient term that is multiplied by terms that depend on the rotor position resulting from the second term in (40):

$$T_e\,(\theta_{rm}) = T_L + T_{e0}\,(T_{e1}\,(\theta_{rm}) + T_{e2}\,(\theta_{rm})) \tag{42}$$

where T_L, T_{e0}, T_{e1}, and T_{e2} are given by

$$T_L = \frac{9}{4} I_s^2 P_r L_{ac} \sin(2\phi_i) \tag{43}$$

$$T_{e0} = \frac{\sqrt{2}}{4}\frac{I_s P_r \pi r_{st}\, l N_{pc} f_{pm,n}}{n}$$

$$\times \left(w_{\left(n\frac{P_r}{P_s}\right)} p_{dc} + \frac{1}{2} w_{\left(\frac{S_s - \frac{P_r}{2}}{\frac{P_s}{2}}\right)} p_{ac.j} \right) \quad (44)$$

$$T_{e1}(\theta_{rm}) = \left(1 + 2\cos\left(\left(\gamma n \frac{P_r}{P_s} + 1\right)\frac{2\pi}{3}\right)\right) \times \cos\left((n+1)\frac{P_r}{2}\theta_{rm} + \phi_i\right) \quad (45)$$

$$T_{e2}(\theta_{rm}) = \left(1 + 2\cos\left(\left(\gamma n \frac{P_r}{P_s} - 1\right)\frac{2\pi}{3}\right)\right) \times \cos\left((n-1)\frac{P_r}{2}\theta_{rm} + \phi_i\right) \quad (46)$$

To get more insight on (42), Fig. 3 shows the predicted torque waveform versus electrical rotor position θ_r of a sample PMAC machine having a torque ripple percentage of 4.5% considering different harmonic components. It is observed that the dc-component of torque corresponds to the fundamental components of permeance function $j = 2$ in (11) along with its dc component, and permanent magnet MMF $n = 1$ in (6) as shown by the red and blue curves. Also shown therein is that the third and its multiple magnet MMF harmonics do not affect the torque production as indicated by the pink curve coinciding on the x-axis, as was discussed in [27]. In addition, torque ripple is significantly affected by the MMF harmonics $n = 5$ and $n = 7$, contributing to 3.56% and 0.92% to the overall torque ripple percentage, which are indicated by the cyan and black curves. Including only these ripples and adding them to the dc-torque gives a good representation of the overall torque, blue curve, which was calculated considering 100 harmonics. Finally, it is interesting to note that permeance harmonic $j = 4$ and higher have insignificant effect on the produced torque.

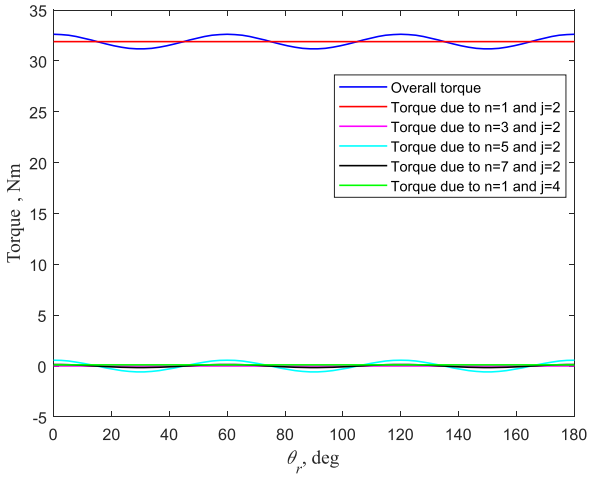

FIGURE 3. Torque waveform expression (42) Vs. electrical rotor position due to different harmonics.

III. MODEL VALIDATION

In this section, the developed model is validated numerically and experimentally. Fig. 4 (a) shows a cross section of a Y-connected 4.9 kW, 1500 rpm, 18-slot, 14-pole SM fractional slot concentrated winding PMSM (FSCW-PMSM). Details on the machine geometry, magnet, winding and applied current are given in Table 1, where I_{rated} is the rated line current, V_{rated} is the rated line-line voltage, P_{rated} is the rated output power, T_{rated} is the rated torque, and ω_{rated} is the rated speed. The winding function harmonic coefficient for this machine is given in the first row of Table 2.

This machine is equipped with NdFeB magnets with a residual flux density equal to 1.33 T. It also utilizes two parallel groups of windings with double layer configuration as shown in Fig. 4 (b). The line current from the inverter is divided equally into each group. For example, group 1 in the *a*-phase consists of coils C1, C2, and C3 representing the coils between slots 6 and 5, slots 5 and 4, and slots 1 and 18, respectively. Group 2 consists of the coils C4, C5, and C6 representing the coils between slots 15 and 14, slots 13 and 14, and slots 9 and 10, respectively. The return path of the current from both the groups is connected to the neutral in a Y- configuration.

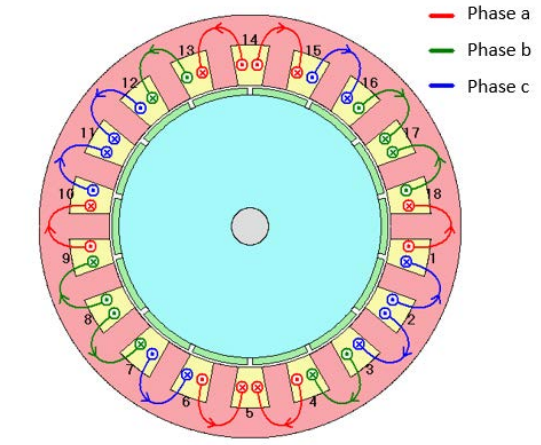

(a)

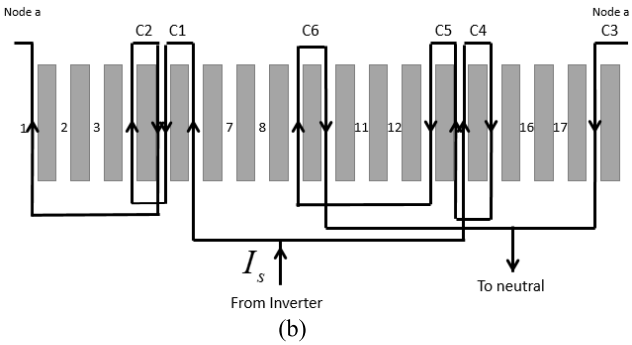

(b)

FIGURE 4. (a) Cross section of an 18 slot 14 pole FSCW-PMSM (b) Winding layout for a-phase.

A. 2-D FEA VALIDATION

The analytical model developed was used to predict the inductances, torque, no-load back-emf and airgap flux density of this machine and the results were then compared to ones

TABLE 1. Machine characteristics.

Parameter	Value	Parameter	Value
S_s	18	d_{sb}	12.0 mm
P_r	14	w_{tb}	14.3 mm
N_{pc}	51 turns	α_{pm}	0.92
n_{pw}	2	α_t	0.52
l	60.0 mm	B_r	1.33 T
r_{rs}	21.0 mm	I_{rated}	11.5 A
d_i	43.8 mm	ϕ_i	8.6 degrees
d_{rb}	9.67 mm	V_{rated}	270 V
d_m	4.0 mm	P_{rated}	4948 W
g	1.5 mm	T_{rated}	32.5 Nm
d_{tb}	23.0 mm	ω_{rated}	1500 rpm

TABLE 2. Winding function Fourier series coefficient.

Slots and Poles	w_k
FSCW-PMAC machine $S_s=18, P_r=14, P_s=2$	$\frac{4N_{pc}}{k\pi}\left(\begin{array}{l}\frac{1}{2}\sin\left(k\frac{\pi}{2}\left(\frac{P_s}{S_S}\right)\right)\\ +\frac{1}{2}\sin\left(k\frac{\pi}{2}\left(\frac{5P_s}{S_S}\right)\right)\end{array}\right)$
Vernier Machine $S_s=18, P_r=30, P_s=6$	$\frac{4N_{pc}}{k\pi}\sin\left(\frac{k\pi}{2}\right)\left(\begin{array}{l}\cos\left(\frac{k}{2}\left(\pi-\frac{2\pi P_s}{S_S}\right)\right)\\ -2\sin\left(k\frac{\pi P_s}{S_S}\right)^2\end{array}\right)$

obtained numerically using a 2-D ANSYS Maxwell FEA software [33]. To get a better insight on the applicability of the model for wide and thin teeth, different values of magnet span and tooth span, α_{pm} and α_t, respectively, were selected as shown in Table 3. As can be seen, the results from the model match well with those predicted from the FEA model in terms of self-inductance and torque for various α_{pm} and α_t. Note that due to the concentrated winding configuration this machine employs, the mutual inductance between any two phases is small and almost zero; which is confirmed using (29) for *a*- phase and *b*-phase. It is noteworthy to point out that if in (16) the airgap was assumed uniform, the analytical model predicted *a*- phase average self-inductance value would be around 1.66 mH, 2.4 mH, and 3.22 mH, respectively; for the three cases shown in Table 3; which shows that such assumption can introduce some error in the predictions.

Fig. 5 shows the torque waveforms as a function of electrical rotor position predicted using FEA and the developed analytical model under full rated torque (op1), 75% rated torque (op2) and 50% rated torque (op3). All points operate at a rotor speed of 1500 rpm with $\alpha_{pm} = 0.92$ and $\alpha_t = 0.52$. The torque ripple percentage from the FEA and

TABLE 3. FEA validation of average self-inductances.

(α_t, α_{pm})	Method	a- phase (mH)	b- phase (mH)	c- phase (mH)	Torque (Nm)
(0.3,0.5)	Analytical	1.01	1.01	1.02	21.38
	FEA	0.92	0.92	0.93	20.97
(0.52,0.92)	Analytical	2.26	2.27	2.27	32.20
	FEA	2.19	2.21	2.20	31.40
(0.9,0.7)	Analytical	2.51	2.51	2.52	38.23
	FEA	2.48	2.48	2.48	37.56

analytical models are found to be 0.91% and 0.75% for op1, 0.90% and 0.74% for op2, and 0.93% and 0.76% for op3, respectively. Nevertheless, a good match in results can be seen.

It is noted that the predicted error increases as the excitation level increases, and that the predicted analytical torque is higher than that of the FEA This error stems from the assumption made in the analytical model which ignores the tangential component in the airgap flux density and assumes all of the flux density in the airgap is radial. As the excitation level keeps increasing, the tangential component in the airgap increases. The analytical model assumes that all flux density in the airgap is radial and uses that to calculate the torque, which results in overestimation when compared to FEA torque.

The airgap flux density under full rated torque is shown in Fig. 6. It is observed that slotting effects are captured with good accuracy.

B. EXPERIMENTAL VALIDATION

Experimental verification was carried out using the test-setup shown in Fig. 7 and with the parameters listed in Table 1. This setup consisted of a Y-configured PMSM coupled to a DC machine. The DC machine acts as generator and the output of which is connected to a resistive load. The PMSM is powered from an electronic variable frequency drive which generates the three-phase PWM signal in an open-loop mode. A torque sensor, rated at 100 Nm, 10000 rpm and with sensitivity of 50 mV/Nm, mounted on the shaft is used for torque measurement. The machine stator inductance is measured using an LCR meter.

Table 4 shows a comparison of the average torque values obtained analytically and experimentally for the three aforementioned operating points. Note that due to equipment limitations, torque ripple could not be measured. Good agreement in results can be seen. The experimentally measured *a*-phase self-inductance was equal to 2.20 mH which is close to the analytical model predicted value of 2.26 mH shown in Table 3. The no-load back-emf waveforms at the rated conditions obtained from the analytical model, FEA and experimental measurement are shown in Fig. 8 where it is noted that the back-emf is sinusoidal for these conditions. Good agreement in results is seen.

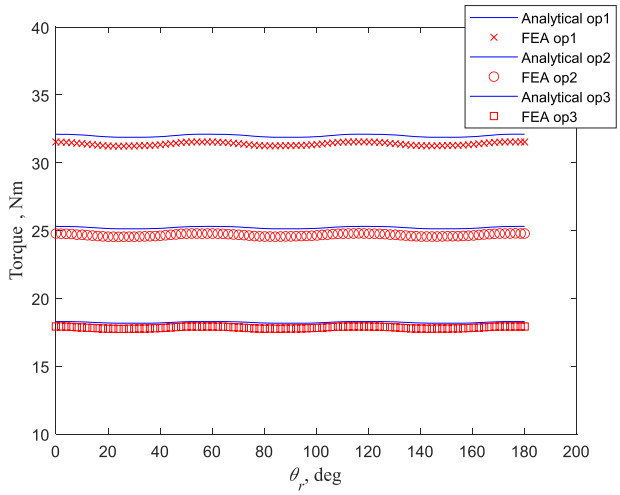

FIGURE 5. Analytical and FEA Torque for the three operating point using $\alpha_{pm} = 0.92$ and $\alpha_t = 0.52$.

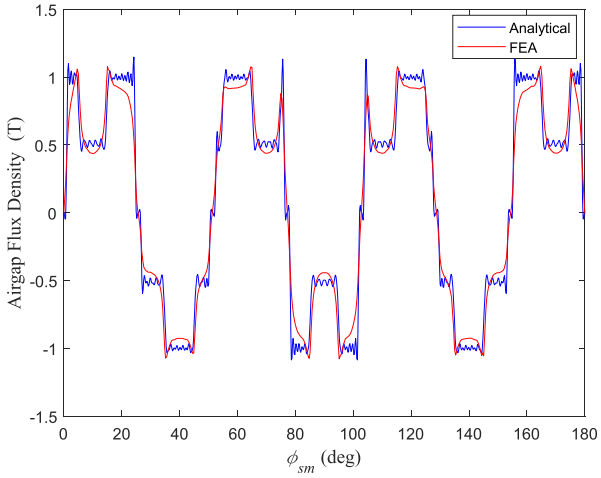

FIGURE 6. Analytical and FEA Airgap flux density at the rated condition using $\alpha_{pm} = 0.92$ and $\alpha_t = 0.52$.

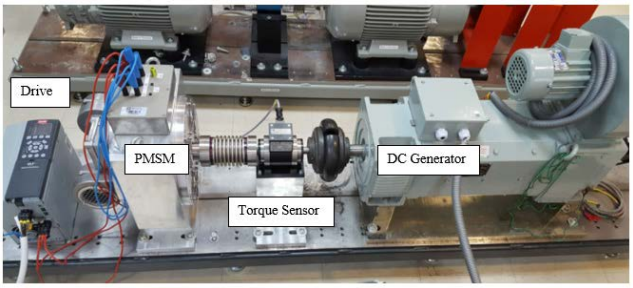

FIGURE 7. Experimental test setup 18 slot 14 pole FSCW-PMSM.

C. 2-D FEA VALIDATION WITH NON-SINUSOIDAL BACK-EMF

As can be inferred from (33), the back-emf harmonics content becomes significant based on a number of conditions such as the winding topology applied which affects the winding function and therefore the amplitude of the winding function harmonic coefficients, and the slot and poles combination. Based on this, an FEA model with magnet poles equal to 30 and with α_t and α_{pm} set 0.5 and 0.7, respectively; was built. The rest of the machine parameters are unchanged as listed in Table 1 while the winding configuration applied has the winding function harmonics coefficient listed in row 2 of Table 2. With the new number of magnet and stator poles, the Vernier effect is satisfied and hence the machine is classified as a Vernier machine [34], [35], [36], [37].

Fig. 9 shows the back-emf obtained from the developed model and FEA. As shown, the back-emf is non-sinusoidal due to the existence of significant higher order harmonics in (33). The analytically predicted average torque, torque ripple percentage and a-phase self-inductance at θ_{rm} equals to zero were calculated at 15.55 Nm, 0.8%, and 8.78 mH, respectively. The same values obtained from FEA were found to be 14.75 Nm, 1.1%, and 8.12 mH; respectively. The increased error in the average torque prediction compared to the results in sub-sections A and B is due to the relatively more magnet-magnet leakage present in Vernier machine compared to FSCW-PMSM.

TABLE 4. Comparison of average torque.

Operating Point	Analytical (Nm)	Experimental (Nm)
op1	32.20	31.20
op2	25.28	24.51
op3	18.18	17.75

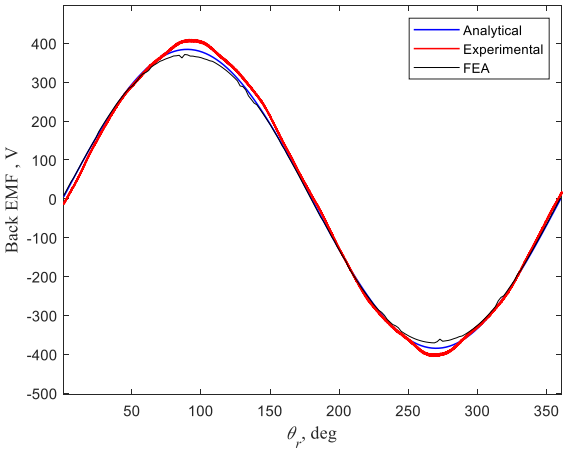

FIGURE 8. No-load back-emf at the rated speed (a-phase).

IV. APPLICATION TO OPTIMIZATION DESIGN

The developed analytical model was integrated into an evolutionary optimization design algorithm with the purpose of designing a 1.86 kW PMSM with a 5:1 constant power speed range (CPSR) [27]. In this design, three torque-speed operating points were modeled to capture the flux weakening

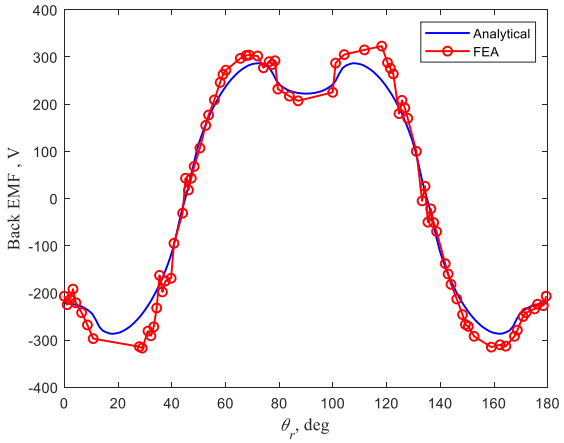

FIGURE 9. Non-sinusoidal back-emf at the rated conditions (*a*-phase).

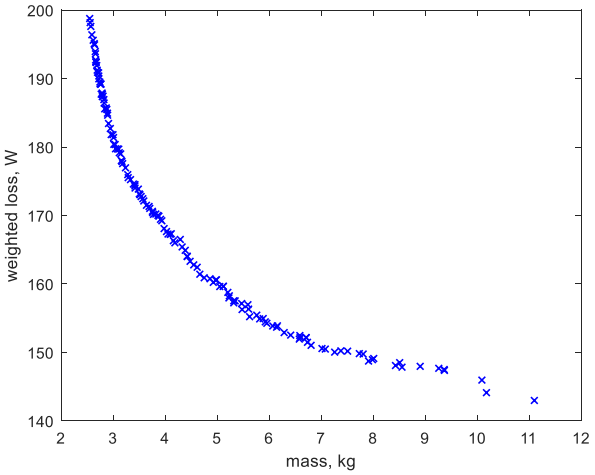

FIGURE 10. Pareto optimal front.

region [27]. A total of 20 design parameters/degrees of freedom were used [27]. Ten of these parameters were geometrical and winding parameters, four were used to select the material of the stator, rotor, magnets, and conductors; and the last six were the stator current rms value and current angle for each operating point [27]. A total of 18 hard constraints were applied and two optimization objectives were set to be minimized which were the total machine electromagnetic mass and total weighted loss computed from the three points. The total weighted loss includes the winding conduction loss, core loss, magnet loss and conduction loss in the inverter.

Recently, various promising evolutionary optimization algorithms such as Garra Rufa, Gray Wolves, and Dragonfly have been proposed for various applications aiming to improve the computational speed of the optimization [38], [39], [40]. Integrating the developed model in one of these modern algorithms will be an interesting investigation in terms of convergence speed. It is therefore important to have a benchmark reference to compare with. For this purpose, the developed model is encapsulated into the classical well-known genetic algorithm (GA) toolbox [41]. The number of stator slots, stator poles and rotor poles were fixed at 18, 2, and 14; respectively. A concentrated winding topology is adopted as described in [27]. More information about this design procedure can be found in [27].

The optimization was run for a GA population of 500 and generation of 500. The resulting trade-off curve between the defined objectives, better known as the Pareto-optimal front, is shown in Fig. 10, where the x-axis represents the total electromagnetic mass of the machine and y- axis gives the total weighted power loss. Each point in this curve is a separate machine design that satisfied all imposed constraints. For example, the lowest achievable machine electromagnetic mass during the optimization was found to be 2.8 kg. This machine has weighted power loss of around 190 W. Similarly, the heaviest machine has an electromagnetic mass of around 11.2 kg with weighted power loss of 145 W. It can be deduced that higher mass machines are more efficient (less weighted loss) due to the increase in the stator mass to reduce conduction and core loss happening in the stator region, but at the expense of heavier machines.

A total of 147 machines were designed as shown in Fig. 10, where the optimization took around one hour on an i-5 desktop PC with 8 GB-ram, 3.0 GHz processor, and 8 cores, which involved 1.2 million evaluations of the analytical model script. Similar design procedures using numerical methods with much smaller space require much more computational time [5], [6], [37].

To assert the computational effectiveness of the developed model, it was run using 300 winding function harmonics k in (2), 300 magnet MMF harmonics n in (5), and 300 airgap permeance harmonics j in (9). Moreover, 1200 points were considered, in the span of zero to 2π, for ϕ_{sm}. The analytical script was run for one rotor position corresponding to θ_{rm} equal to zero. To make the comparison as fair as possible, two magneto-static linear FEA studies were conducted for the same rotor position: the first incorporated adaptive meshing with three pass/adaptions; while the second did not incorporate adaptive meshing and was relying on the initial mesh. By running the studies on an i-5 desktop PC with 3.0 GHz and 8 processing cores, it was found that the analytical script took 0.025 seconds to obtain the electromagnetic field solutions, compared to 15 seconds and 9 seconds for the first and second FEA studies, respectively. It should be noted that this time does not include the time needed to build the machine geometry or its winding in the analytical or FEA software.

V. CONCLUSION AND FUTURE WORK

This work presents a novel *abc*-variable based analytical model for surface-mounted PMAC machines which can be utilized to predict the electromagnetic machine performance with a sinusoidal or non-sinusoidal back-emf. Closed-form expressions for important parameters such as inductances, flux linkages, and torque were presented. Validation of the model was done using FEA and experimental tests on a lab-prototype, where a good match in results was demonstrated for sinusoidal and non-sinusoidal back-emf. In particular,

it was shown that for a PMAC machine with sinusoidal back-emf, the maximum error in the average torque between the developed model and 2-D FEA, and the developed model and experimental results is 2.51% and 3.15%, respectively. For the machine with non-sinusoidal back-emf, the error in the average torque between the developed model and 2-D FEA is 5.28%. Finally, the computational effectiveness of the model in a multi-objective evolutionary optimization setting was demonstrated.

Future work includes further testing under different operating conditions and in particular under the field-weakening region. The model can be further enhanced by adapting it to the presence of stator tooth-tips. This work can be expanded to model non-linear effects especially in the stator teeth. Finally, the inclusion of cogging torque prediction can be considered.

REFERENCES

[1] J.-W. Jung, K.-T. Jung, B.-H. Lee, and J.-P. Hong, "Design and analysis of ferrite magnet flux concentrated PMSM with cross-laminated rotor core using equivalent 2-D FEA," *IEEE Trans. Energy Convers.*, vol. 34, no. 3, pp. 1623–1631, Sep. 2019, doi: 10.1109/TEC.2019.2897575.

[2] R. Dutta, A. Pouramin, and M. F. Rahman, "A novel rotor topology for high-performance fractional slot concentrated winding interior permanent magnet machine," *IEEE Trans. Energy Convers.*, vol. 36, no. 2, pp. 658–670, Jun. 2021, doi: 10.1109/TEC.2020.3030302.

[3] Y. Demir, A. M. EL-Refaie, and M. Aydin, "Investigation of asymmetric and unbalanced winding structures for 3-phase permanent magnet synchronous machines," *IEEE Trans. Energy Convers.*, vol. 36, no. 3, pp. 1722–1732, Sep. 2021, doi: 10.1109/TEC.2020.3044000.

[4] P. Eklund, J. Sjolund, M. Berg, M. Leijon, and S. Eriksson, "Experimental evaluation of a rare earth-free permanent magnet generator," *IEEE Trans. Energy Convers.*, vol. 36, no. 1, pp. 3–10, Mar. 2021, doi: 10.1109/TEC.2020.3000594.

[5] R. Zhang, J. Li, R. Qu, and D. Li, "Analysis and design of triple-rotor axial-flux spoke-array Vernier permanent magnet machines," *IEEE Trans. Ind. Appl.*, vol. 54, no. 1, pp. 244–253, Jan. 2018, doi: 10.1109/TIA.2017.2764448.

[6] M. S. Islam, R. Mikail, R. Chattopadhyay, and I. Husain, "A 3D-airgap slotless permanent magnet machine for transportation applications," in *Proc. IEEE Energy Convers. Congr. Exposit. (ECCE)*, Oct. 2020, pp. 35–40, doi: 10.1109/ECCE44975.2020.9236026.

[7] N. Bernard, R. Missoum, L. Dang, N. Bekka, H. B. Ahmed, and M. E.-H. Zaim, "Design methodology for high-speed permanent magnet synchronous machines," *IEEE Trans. Energy Convers.*, vol. 31, no. 2, pp. 477–485, Jun. 2016, doi: 10.1109/TEC.2015.2513669.

[8] W. Tong, S. Li, X. Pan, S. Wu, and R. Tang, "Analytical model for cogging torque calculation in surface-mounted permanent magnet motors with rotor eccentricity and magnet defects," *IEEE Trans. Energy Convers.*, vol. 35, no. 4, pp. 2191–2200, Dec. 2020, doi: 10.1109/TEC.2020.2995902.

[9] W. Tong, S. Wang, S. Dai, S. Wu, and R. Tang, "A quasi-three-dimensional magnetic equivalent circuit model of a double-sided axial flux permanent magnet machine considering local saturation," *IEEE Trans. Energy Convers.*, vol. 33, no. 4, pp. 2163–2173, Dec. 2018, doi: 10.1109/TEC.2018.2853265.

[10] Z. Frank and J. Laksar, "Analytical design of coreless axial-flux permanent magnet machine with planar coils," *IEEE Trans. Energy Convers.*, vol. 36, no. 3, pp. 2348–2357, Sep. 2021, doi: 10.1109/TEC.2021.3050502.

[11] G. Liu, L. Liu, Q. Chen, and W. Zhao, "Torque calculation of five-phase interior permanent magnet machine using improved analytical method," *IEEE Trans. Energy Convers.*, vol. 34, no. 2, pp. 1023–1032, Jun. 2019, doi: 10.1109/TEC.2018.2880574.

[12] H. Fang and D. Wang, "A novel design method of permanent magnet synchronous generator from perspective of permanent magnet material saving," *IEEE Trans. Energy Convers.*, vol. 32, no. 1, pp. 48–54, Mar. 2017, doi: 10.1109/TEC.2016.2621133.

[13] E. Devillers, J. Le Besnerais, T. Lubin, M. Hecquet, and J.-P. Lecointe, "A review of subdomain modeling techniques in electrical machines: Performances and applications," in *Proc. 32nd Int. Conf. Electr. Mach. (ICEM)*, Sep. 2016, pp. 86–92, doi: 10.1109/ICELMACH.2016.7732510.

[14] K. Boughrara, N. Takorabet, R. Ibtiouen, O. Touhami, and F. Dubas, "Analytical analysis of cage rotor induction motors in healthy, defective, and broken bars conditions," *IEEE Trans. Magn.*, vol. 51, no. 2, pp. 1–17, Feb. 2015, doi: 10.1109/TMAG.2014.2349480.

[15] Y. Liu, B. Zhang, M. Zong, G. Feng, and B. Gan, "Magnetic field prediction of module-combined stator permanent magnet synchronous motor based on a nonlinear hybrid analytical model," *IEEE Access*, vol. 9, pp. 122486–122494, 2021, doi: 10.1109/ACCESS.2021.3109262.

[16] Z. Li, X. Huang, Z. Chen, L. Wu, Y. Shen, and T. Shi, "Electromagnetic analysis for interior permanent-magnet machine using hybrid subdomain model," *IEEE Trans. Energy Convers.*, vol. 37, no. 2, pp. 1223–1232, Jun. 2022, doi: 10.1109/TEC.2021.3112813.

[17] D. Golovanov and C. Gerada, "Analytical methodology for modelling of circulating current loss in synchronous electrical machines with permanent magnets," *IEEE Trans. Energy Convers.*, vol. 37, no. 1, pp. 220–231, Mar. 2022, doi: 10.1109/TEC.2021.3091811.

[18] S. D Sudhoff, *Power Magnetic Devices: A Multi-Objective Design Approach*. Hoboken, NJ, USA: Wiley, Feb. 2014.

[19] H. Dhulipati, S. Mukundan, C. Lai, K. Mukherjee, J. Tjong, and N. C. Kar, "Multiple reference frame-based extended concentrated wound PMSM model considering PM flux linkage and inductance harmonics," *IEEE Trans. Energy Convers.*, vol. 34, no. 2, pp. 731–740, Jun. 2019, doi: 10.1109/TEC.2018.2880869.

[20] F. Kutt, M. Michna, and G. Kostro, "Multiple reference frame theory in the synchronous generator model considering harmonic distortions caused by nonuniform pole shoe saturation," *IEEE Trans. Energy Convers.*, vol. 35, no. 1, pp. 166–173, Mar. 2020, doi: 10.1109/TEC.2019.2951858.

[21] H. Atighechi, S. Chiniforoosh, S. Ebrahimi, and J. Jatskevich, "Using multiple reference frame theory for considering harmonics in average-value modeling of diode rectifiers," *IEEE Trans. Energy Convers.*, vol. 31, no. 3, pp. 872–881, Sep. 2016, doi: 10.1109/TEC.2016.2536706.

[22] G. Feng, C. Lai, J. Tian, and N. C. Kar, "Multiple reference frame based torque ripple minimization for PMSM drive under both steady-state and transient conditions," *IEEE Trans. Power Electron.*, vol. 34, no. 7, pp. 6685–6696, Jul. 2019, doi: 10.1109/TPEL.2018.2876607.

[23] H. Zhang, M. Dou, and J. Deng, "Loss-minimization strategy of nonsinusoidal back EMF PMSM in multiple synchronous reference frames," *IEEE Trans. Power Electron.*, vol. 35, no. 8, pp. 8335–8346, Aug. 2020, doi: 10.1109/TPEL.2019.2961689.

[24] G. Hong, T. Wei, and X. Ding, "Multi-objective optimal design of permanent magnet synchronous motor for high efficiency and high dynamic performance," *IEEE Access*, vol. 6, pp. 23568–23581, 2018, doi: 10.1109/ACCESS.2018.2828802.

[25] S. G. Min and B. Sarlioglu, "Fast and systematic design optimization of surface-mounted PM machines using advanced analytical models and subharmonic elimination methods," *IEEE Trans. Magn.*, vol. 55, no. 1, pp. 1–16, Jan. 2019, doi: 10.1109/TMAG.2018.2877403.

[26] S. G. Min, "Analytical design and optimization of axial flux permanent magnet machines with slotless structure," *IEEE Trans. Transport. Electrific.*, vol. 8, no. 2, pp. 1994–2004, Jun. 2022, doi: 10.1109/TTE.2021.3124258.

[27] S. O. Edhah, J. Y. Alsawalhi, and A. A. Al-Durra, "Multi-objective optimization design of fractional slot concentrated winding permanent magnet synchronous machines," *IEEE Access*, vol. 7, pp. 162874–162882, 2019, doi: 10.1109/ACCESS.2019.2951023.

[28] J. Y. Alsawalhi and S. D. Sudhoff, "Design optimization of asymmetric salient permanent magnet synchronous machines," *IEEE Trans. Energy Convers.*, vol. 31, no. 4, pp. 1315–1324, Dec. 2016, doi: 10.1109/TEC.2016.2575138.

[29] Z. Q. Zhu and D. Howe, "Instantaneous magnetic field distribution in brushless permanent magnet DC motors. III. Effect of stator slotting," *IEEE Trans. Magn.*, vol. 29, no. 1, pp. 143–151, Jan. 1993, doi: 10.1109/20.195559.

[30] M. Choi and B. Kim, "Calculation of PM Vernier motors using an improved air-gap permeance function," *IEEE Trans. Magn.*, vol. 55, no. 6, pp. 1–5, Jun. 2019, doi: 10.1109/TMAG.2019.2901541.

[31] S. O. Edhah and J. Y. Alsawalhi, "Air gap flux density analytical model for a fractional-slot concentrated-winding SM-PMSM," in *Proc. IEEE Int. Conf. Electr. Syst. Aircr., Railway, Ship Propuls. Road Vehicles Int. Transp. Electrific. Conf. (ESARS-ITEC)*, Nov. 2018, pp. 1–6, doi: 10.1109/ESARS-ITEC.2018.8607653.
[32] O. Laldin, S. D. Sudhoff, and S. Pekarek, "Modified Carter's coefficient," *IEEE Trans. Energy Convers.*, vol. 30, no. 3, pp. 1133–1134, Sep. 2015.
[33] *ANSYS Maxwell*. Accessed: Oct. 3, 2021. [Online]. Available: http://www.ansys.com/
[34] Q. Lin, S. Niu, and W. N. Fu, "Design and optimization of a dual-permanent-magnet Vernier machine with a novel optimization model," *IEEE Trans. Magn.*, vol. 56, no. 3, pp. 1–5, Mar. 2020, doi: 10.1109/TMAG.2019.2956071.
[35] H. Ahmad and J.-S. Ro, "Analysis and design optimization of V-shaped permanent magnet Vernier motor for torque density improvement," *IEEE Access*, vol. 9, pp. 13542–13552, 2021, doi: 10.1109/ACCESS.2021.3052258.
[36] S. Jia, K. Yan, D. Liang, R. Qu, J. Liu, and J. He, "A novel DC-biased current dual PM Vernier machine," *IEEE Trans. Ind. Appl.*, vol. 57, no. 5, pp. 4595–4605, Sep. 2021, doi: 10.1109/TIA.2021.3084544.
[37] L. Xu, W. Wu, W. Zhao, G. Liu, and S. Niu, "Robust design and optimization for a permanent magnet Vernier machine with hybrid stator," *IEEE Trans. Energy Convers.*, vol. 35, no. 4, pp. 2086–2094, Dec. 2020, doi: 10.1109/TEC.2020.3011925.
[38] A. S. Jaber, H. A. Abdulbari, N. A. Shalash, and A. N. Abdalla, "Garra Rufa-inspired optimization technique," *Int. J. Intell. Syst.*, vol. 35, no. 11, pp. 1831–1856, 2020.
[39] S. Mirjalili, S. M. Mirjalili, and A. Lewis, "Grey wolf optimizer," *Adv. Eng. Softw.*, vol. 69, pp. 46–61, Mar. 2014.
[40] S. Mirjalili, "Dragonfly algorithm: A new meta-heuristic optimization technique for solving single-objective, discrete, and multi-objective problems," *Neural Comput. Appl.*, vol. 27, no. 4, pp. 1053–1073, May 2016.
[41] (Nov. 2017). *Genetic Optimization System Engineering Tool (GOSET) for Use With MATLAB*. [Online]. Available: https://engineering.purdue.edu/ECE/Research/Areas/PEDS/go_system_engineering_toolbox

SALEH O. EDHAH (Student Member, IEEE) received the B.S. and M.S. degrees in electrical engineering from Khalifa University, United Arab Emirates, in 2016 and 2018, respectively, where he is currently pursuing the Ph.D. degree.

JAMAL Y. ALSAWALHI (Senior Member, IEEE) received the B.S., M.S., and Ph.D. degrees in electrical engineering from Purdue University, in 2009, 2011, and 2014, respectively. He is currently an Assistant Professor in electrical engineering with Khalifa University, United Arab Emirates. His research interests include design and analysis of electrical machines and wireless power transfer systems and application of evolutionary optimization design techniques all directed toward the application of transportation electrification.

ABDUL R. BEIG (Senior Member, IEEE) received the B.E. degree in electrical engineering from the National Institute of Technology Karnataka, Suratkal, India, in 1989, and the M.Tech. and Ph.D. degrees in electrical engineering from the Indian Institute of Science, Bengaluru, India, in 1998 and 2004, respectively. He is currently working as an Associate Professor with the Electrical Engineering and Computer Science Department, Khalifa University, Abu Dhabi, United Arab Emirates. His current research interests include auto tuning of grid connected converters, energy management and drive train in electric vehicles, modular multi-level converter for HVDC applications, high power drives, and SiC and GaN-based converters.